

# 2.5-Dimensional Electrical Resistivity Tomography for Cylindrical Objects Incorporating the Modified Optimization Wavenumbers

Lan Gao<sup>1</sup>, Xiaodong Yang<sup>2</sup>, Hongwei Zhou<sup>3</sup>, Mingxin Yue<sup>4</sup>, Bowen Chen<sup>5</sup>, Daiming Hu<sup>6</sup>,  
and Xiaoping Wu<sup>7</sup>

<sup>1</sup>+86 15527735755

<sup>2</sup>+86 19855190635

<sup>3</sup>+86 15927290963

<sup>4</sup>+86 18226632295

<sup>5</sup>+86 18643147360

<sup>6</sup>+86 18756549505

<sup>7</sup>+86 13675517969

November 24, 2022

## Abstract

More and more applications of electrical resistivity tomography (ERT) for cylindrical objects have been rising in recent decades. This paper presents a 2.5-dimensional differential resistivity reconstruction scheme of cylindrical objects. The forward modeling algorithm incorporates the modified optimization wavenumbers to achieve an accurate 2.5-dimensional forward modeling. The modified optimization wavenumber selection is based on the approximate analytic solution of the circumference potential distribution of an infinitely long homogeneous cylindrical model, making it more accurate for cylindrical objects compared to the traditional optimization wavenumber selection which is only applicable for the half-space condition. In the laboratory, we measured the resistivity and resistance distributions of the sodium chloride solution-filled cylindrical tanks with/without a high resistivity rubber bar in the central. The modified and traditional optimization wavenumbers are included respectively to calculate the resistance distribution of the measured objects. The comparison results between the calculated and measured resistance distribution show that the modified optimization wavenumbers proposed in this paper can obtain higher calculation accuracy. The differential ERT incorporating the modified optimization wavenumbers is then employed to reconstruct the resistivity distribution of the cylindrical objects. The inversed resistivity values are in good agreement with the measured values. We, therefore, conclude that the modified optimization wavenumbers can result in better accuracy than the traditional one and the proposed 2.5-dimensional differential resistivity reconstruction scheme is time-saving and has great promise for the imaging of cylindrical objects.

1           **2.5-Dimensional Electrical Resistivity Tomography for Cylindrical Objects**  
2           **Incorporating the Modified Optimization Wavenumbers**  
3

4 **Lan Gao<sup>1,2</sup>, Xiaodong Yang<sup>1,2,3</sup>, Hongwei Zhou<sup>4</sup>, Mingxin Yue<sup>1,2,3</sup>, Bowen Chen<sup>1,2</sup>, Daiming**  
5 **Hu<sup>1,2</sup>, Xiaoping Wu<sup>1,2,3\*</sup>**

6 <sup>1</sup> Univ Sci & Technol China, Sch Earth & Space Sci, Hefei 230026, Peoples R China

7 <sup>2</sup> CAS Ctr Excellence Comparat Planetol, Hefei 230026, Peoples R China

8 <sup>3</sup> Univ Sci & Technol China, Mengcheng Natl Geophys Observ, Hefei 230026, Peoples R China

9 <sup>4</sup> Hubei Key Laboratory of Earthquake Early Warning, Institute of Seismology, CEA, Wuhan  
10 Institute of Earthquake Engineering Co. Ltd. 40 Hongshance Road, Wuhan, China, 430071.

11  
12 Corresponding author: Xiaoping Wu (wxp@ustc.edu.cn.)  
13

14 **Key Points:**

- 15       • We present a 2.5-dimensional ERT scheme for cylindrical objects incorporating the  
16       modified optimization wavenumbers.  
17       • The modified optimization wavenumber selection based on the analytic solution of an  
18       infinitely long homogeneous cylinder is firstly analyzed.  
19       • Both numerical analysis and laboratory experiments prove that the modified optimization  
20       wavenumbers can achieve higher computing accuracy.

21 **Abstract**

22 More and more applications of electrical resistivity tomography (ERT) for cylindrical objects have  
23 been rising in recent decades. This paper presents a 2.5-dimensional differential resistivity  
24 reconstruction scheme of cylindrical objects. The forward modeling algorithm incorporates the  
25 modified optimization wavenumbers to achieve an accurate 2.5-dimensional forward modeling.  
26 The modified optimization wavenumber selection is based on the approximate analytic solution of  
27 the circumference potential distribution of an infinitely long homogeneous cylindrical model,  
28 making it more accurate for cylindrical objects compared to the traditional optimization  
29 wavenumber selection which is only applicable for the half-space condition. In the laboratory, we  
30 measured the resistivity and resistance distributions of the sodium chloride solution-filled  
31 cylindrical tanks with/without a high resistivity rubber bar in the central. The modified and  
32 traditional optimization wavenumbers are included respectively to calculate the resistance  
33 distribution of the measured objects. The comparison results between the calculated and measured  
34 resistance distribution show that the modified optimization wavenumbers proposed in this paper  
35 can obtain higher calculation accuracy. The differential ERT incorporating the modified  
36 optimization wavenumbers is then employed to reconstruct the resistivity distribution of the  
37 cylindrical objects. The inversed resistivity values are in good agreement with the measured values.  
38 We, therefore, conclude that the modified optimization wavenumbers can result in better accuracy  
39 than the traditional one and the proposed 2.5-dimensional differential resistivity reconstruction  
40 scheme is time-saving and has great promise for the imaging of cylindrical objects.

41 **Plain Language Summary**

42 Electrical resistivity tomography as a widely used method has been extended to many new  
43 applications that focus on cylindrical objects. Here we analyze the approximate analytic solution  
44 of the circumference potential distribution of an infinitely long homogeneous cylindrical model,  
45 based on which the modified optimization wavenumber selection is derived. By incorporating the  
46 modified optimization wavenumber, we present a 2.5-dimensional differential resistivity  
47 reconstruction scheme for cylindrical objects. Both numerical analysis and laboratory experiments  
48 demonstrate that the modified optimization wavenumber can improve the accuracy of electrical  
49 resistivity modeling and, ERT, together with the modified optimization wavenumber, has great  
50 promise for detecting cylindrical objects such as tree trunks, human organs, and construction  
51 material.

52 **1 Introduction**

53 In the past decades, ERT as a cost-effective method has shown its advantages in many  
54 areas such as landfill management (Augusto et al., 2017; Dumont et al., 2018), thermal energy  
55 monitoring (Hermans et al., 2012; Lesparre et al., 2019), saltwater intrusion mapping (Franco et  
56 al., 2009; Kazakis et al., 2016), hydrology survey (Apostolopoulos, 2008; Coscia et al., 2012), etc.  
57 These applications all share the commonality that the observed objects are half-space conditions.

58 In recent decades, ERT has been applied to many other areas, which focus on cylindrical  
59 objects. For example, Thanh et al. (2006) proposed using ERT method for evaluating grouting  
60 performance after injection. Karhunen et al. (2010) applied ERT for three-dimensional imaging of  
61 concrete and their results including numerical modeling and experiments indicated that ERT might  
62 be a feasible modality for non-destructive evaluation of concrete. Sapkota et al. (2015) presented  
63 an application of ERT for the visualization of a thrombus in blood. Sardeshpande et al. (2016)

64 adopted ERT technique to obtain the mixture distribution across the cross-section of the mixing  
65 vessel. Ren et al. (2017) used ERT to measure the local velocity of shampoo in an in-line pipeline  
66 loop. Ren et al. (2019) investigated the influence of moisture content and water-cement ratio on  
67 resistivities of different kinds of cement specimens by ERT experiment and the results implied that  
68 ERT technique has potential in defect detection and in-situ monitoring in cement mortar. Losso et  
69 al. (2020) used ERT to study seasonal changes in tree trunks. Rao et al. (2021) used ERT to test,  
70 visualize, and evaluate the progress of crystallization processes.

71 The ERT method utilizes a pair of electrodes as transmitters to inject currents and another  
72 pair of electrodes as receivers to measure the responding voltages, which give a comprehensive  
73 discernment of the object. For cylindrical objects, we usually employ the point currents and  
74 reconstruct the resistivity of the cross-section (Bieker et al., 2010; Elliott et al., 2016; Guyot et al.,  
75 2013). Thus the source is three-dimensional but the object is two-dimensional. We call this the  
76 2.5-dimensional ERT. With the increasing applications of ERT in cylindrical objects, the research  
77 corresponding to the 2.5-dimensional inversion algorithm is becoming more and more important.

78 There are mainly two kinds of inversion algorithms for the ERT of cylindrical objects, one  
79 of which is the absolute ERT represented by the Guasi-Newton algorithm (Loke and Barker, 1996).  
80 The absolute ERT usually consists of iterative processes and is theoretically applicable. However,  
81 this technique lacks robustness (Brazey et al., 2022). The other inversion algorithm is the  
82 differential ERT, which is a one-step linearized reconstruction algorithm represented by the  
83 maximum a posteriori approach (Adler and Guardo, 1996 ). It is more robust against modeling  
84 errors and can achieve fast (near real-time) image reconstruction. Therefore the differential ERT  
85 has been applied in many works of literature (Cao et al., 2020; Xu et al., 2011; Zhang et al., 2012).

86 The forward modeling is an essential step of any inversion algorithm (Gao et al., 2020;  
87 Günther et al., 2006). The commonly employed approaches for solving the Laplace equation in  
88 forward modeling include the finite-difference method (Tsili et al., 2000; Wu et al., 2003),  
89 boundary element method (Mukanova B 2018; Xu et al., 1998), finite element method (Ren  
90 Zhengrong 2010; Wu, 2003; Yang et al., 2017), etc. The finite element method has the advantage  
91 of high flexibility, making it suitable for modeling cylindrical objects. For the 2.5-dimensional  
92 ERT, the Fourier transform is employed to convert the three-dimensional cylindrical model into  
93 the two-dimensional cross-sectional circular model. And the inverse Fourier transform is then  
94 applied to convert the potential in the wavenumber domain to the potential in the spatial domain.  
95 The selection of the wavenumbers for the inverse Fourier transform is very important to improve  
96 the accuracy while reducing the calculation time (Xu et al., 2000). The optimization wavenumber  
97 selection (Xu et al., 2000) can achieve very high accuracy for the half-space condition. However,  
98 when referring to the forward modeling of a cylindrical model, its performance has not been  
99 developed yet. Most of the literature directly use the optimization wavenumbers that are calculated  
100 based on half-space condition. In this paper, we analyze the inapplicability of this kind of  
101 optimization wavenumbers on the 2.5-dimensional ERT of cylindrical objects and modify them  
102 for better modeling of cylindrical objects.

103 We firstly introduce briefly the basic theory of the 2.5-dimensional forward modeling of  
104 infinitely long cylindrical models using finite elements on unstructured grids. Secondly, we  
105 analyze the approximate analytic solution of the circumference potential distribution of an  
106 infinitely long homogeneous cylindrical model, based on which the corresponding modified  
107 optimization wavenumbers and the apparent resistivity tomography algorithm are proposed.  
108 Thirdly, by combing the modified optimization wavenumbers, we conduct the differential ERT of

109 a synthetic model. Lastly, an experiment is conducted to prove the accuracy of this 2.5-dimensional  
 110 modified wavenumber selection based resistivity reconstruction method for cylindrical objects  
 111 through comparisons.

## 112 2 Theory

### 113 2.1 The 2.5-dimensional Forward Modeling of Cylindrical Objects

114 The direct current potential obeys the Laplace equation (Rücker et al., 2006)

$$\nabla \cdot [\sigma(x, y, z)\nabla U(x, y, z)] = -I \cdot \delta(x - x_0) \cdot \delta(y - y_0) \cdot \delta(z - z_0) \quad (1)$$

115 where  $\sigma$  represents the conductivity,  $U$  represents the potential, and  $\delta$  represents the Dirac  
 116 function related to the point source. For an infinitely long cylinder extending along the  $y$ -axis with  
 117 center  $(0,0,0)$ , we conduct the Fourier transform to simplify the three-dimensional equation into  
 118 2.5-dimension by converting  $y$  into wavenumber  $\lambda$  and  $U$  into  $V$ . And the Neumann boundary  
 119 condition is employed

$$\left. \frac{\partial U}{\partial \mathbf{n}} \right|_{\Gamma_1} = 0 \quad (2)$$

120 A mesh generator (Persson and Strang, 2004) is used to discretize the solution domain into  
 121 unstructured triangular meshes, this grid type is flexible and allows for local refinement, thus can  
 122 better simulate a round disk model and reduce the number of nodes. The finite element method  
 123 (Coggon, 1971) is applied to solve the equation (1) as

$$\mathbf{K} \cdot \mathbf{V} = \mathbf{I} \quad (3)$$

124 where the system matrix  $\mathbf{K}$  is sparse and symmetric,  $\mathbf{V}$  is a vector consisting of the potentials in  
 125 the wavenumber domain at all nodes and  $\mathbf{I}$  is a vector representing the source distribution. After  
 126 solving equation (3), we conduct the inverse Fourier transform to obtain the potential value

$$U(x, 0, z) = \frac{2}{\pi} \int_0^{+\infty} V(x, \lambda, z) \cdot d\lambda \quad (4)$$

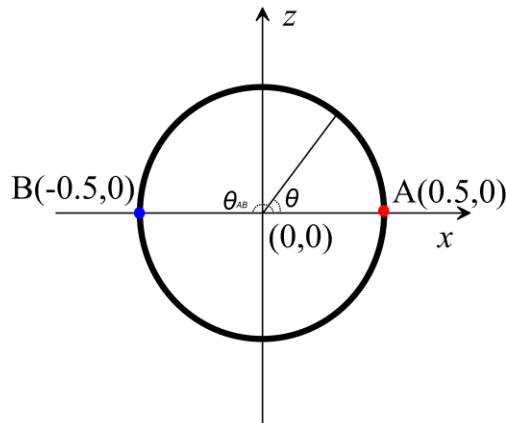
127 Because  $V$  is a series of discrete points and their values change with wavenumbers, which ranges  
 128 from zero to infinity and their relationships are complex, the integral of  $V$  with respect to  
 129 wavenumber  $\lambda$  can not be calculated directly. One approach to solve this problem is to  
 130 approximate (4) as a sum gives

$$U(x, 0, z) = \sum_{j=1}^m V(x, \lambda_j, z) \cdot g_j \quad (5)$$

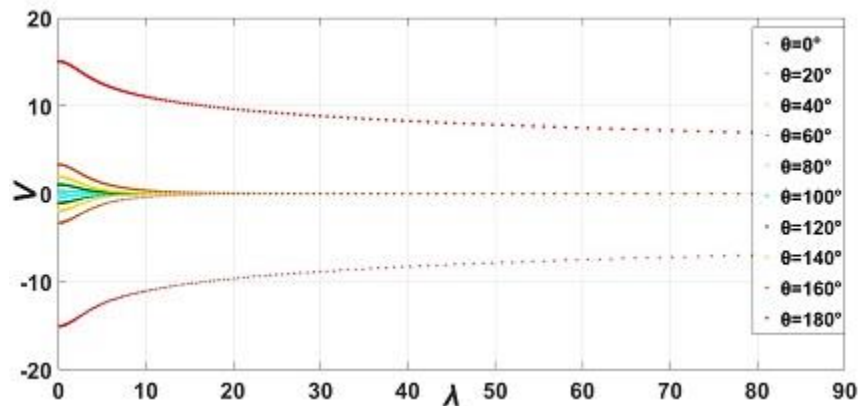
131 where  $m$  is the total wavenumbers,  $\lambda_j$  is the discretized value of  $\lambda$  and  $g_j$  is the corresponding  
 132 weighting coefficient selected by the optimization wavenumber selection method (Xu et al., 2000).  
 133 This traditional optimization wavenumber selection method is frequently used in 2.5-dimensional  
 134 forward modeling of the half-space because of its stability and high accuracy. During the  
 135 wavenumber selection, the author employs  $V$  as  $K_0(\lambda \cdot l)/(2\pi)$ , where  $l$  is the distance between  
 136 the current source and the calculated point and  $K_0$  is the zero-order modified Bessel function of  
 137 the second kind. It is the analytic solution of  $V$  when the model is a homogeneous half-space.  
 138 However, when the object is a cylinder, the analytic solution of  $V$  is definitely different from those

139 of the half-space. Nevertheless, many researches applied the traditional optimization wavenumbers  
 140 to calculate  $\lambda$  and  $g$  directly for the resistivity modeling of cylindrical objects, thus not fitted for  
 141 cylindrical models and can cause great errors.

142 To prove this point of view, we introduce an infinitely long homogeneous cylindrical  
 143 model, as is shown in figure 1, to analyze the relationship between  $V$  and  $\lambda$ , and compare its  $V$  to  
 144 that of the half-space condition. The radius of the cylinder is 0.5m and the resistivity of the cylinder  
 145 is  $600\Omega\cdot\text{m}$ . The two current electrodes A and B are placed on  $(0.5, 0)$  and  $(-0.5, 0)$ , and their  
 146 current intensities are  $-0.02\text{A}$  and  $0.02\text{A}$  respectively.  $\theta_{AB}$  stands for the included angle between  
 147 A and B.  $\theta$  is the included angle between the current electrode A and the measurement point. 201  
 148 wavenumbers ranging from 0.00001 to 81 are employed.



149  
 150 **Figure 1.** The cross section of the homogeneous cylindrical model.

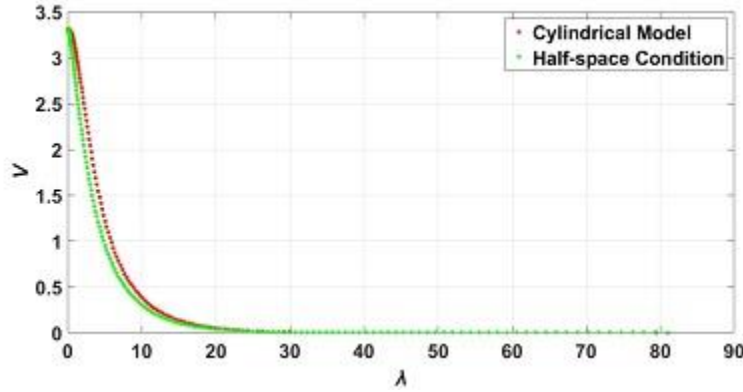


151  
 152 **Figure 2.** The relationship between  $V$  and wavenumber  $\lambda$  on different measurement points.

153 The calculated  $V$  changing with wavenumbers on different points of the circumference are  
 154 shown in figure 2. For a particular point represented by  $\theta$ , its potential  $U$  is the integral of  $V(\lambda)$   
 155 multiply by  $2/\pi$ . When  $\theta$  equals  $0^\circ$  and  $180^\circ$ , the functions  $V(\lambda)$  are not convergent to zero,  
 156 illustrating that the potentials in these two points are infinite. These curves correspond to the fact  
 157 that the potentials in the point sources are infinite.  
 158

159 For a particular point, take  $\theta$  equals  $160^\circ$  as an example. Figure 3 shows the difference of  
 160  $V$  between the cylindrical model and the half-space condition. The difference can influence the

161 wavenumber selection results and finally cause errors in forward modeling. To avoid this in the  
 162 2.5-dimensional simulation of the cylindrical model, the cross-section potential distribution  
 163 should be analyzed in order to modify the optimization wavenumber selection.



164  
 165 **Figure 3.** The difference of  $V$  between the cylindrical model and the half-space condition when  
 166  $\theta$  equals  $160^\circ$ .

## 167 2.2 The Approximate Analytic Solution

168 Because the optimization wavenumber selection method is based on the analytical solution  
 169 of the potential value, we must first analyze the analytic solution of the circumference potential  
 170 distribution of an infinitely long homogeneous cylindrical model. During the numerical simulation,  
 171 for a specific triangle mesh  $e$

$$K_{rs}^e = \sigma_e \left[ \frac{1}{2\Delta} (b_r b_s + c_r c_s) + \frac{\Delta \chi \lambda^2}{6} \right]; s, r = i, j, m; \chi = \begin{cases} 2 & (r = s) \\ 1 & (r \neq s) \end{cases} \quad (6)$$

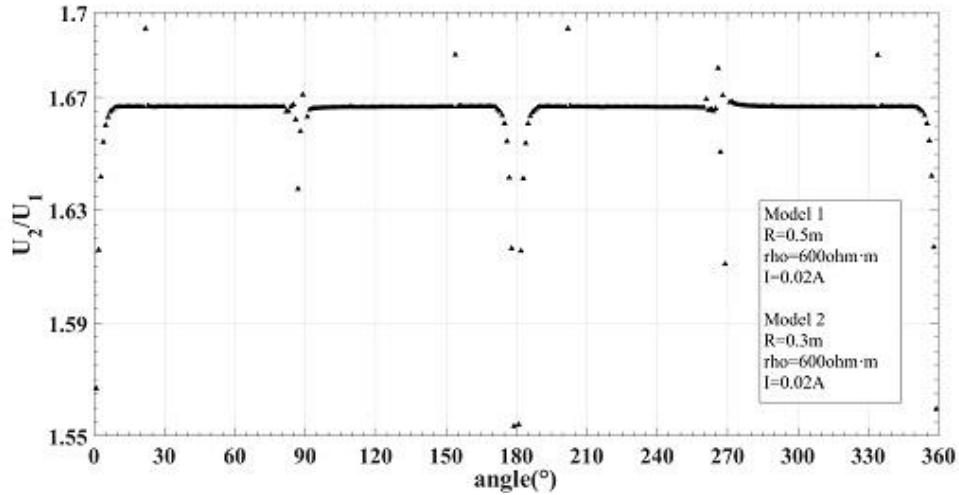
172 where  $i, j, m$  are the numbers of mesh points,  $\Delta$  is the area of the mesh,  $\sigma_e$  is the conductivity, and  
 173  $b$  and  $c$  stand for the coefficients related only to the location of the mesh. Since  $\sigma_e$  is proportional  
 174 to  $\mathbf{K}$  and  $\mathbf{K}$  is inversely proportional to  $\mathbf{V}$ , it can be easily concluded that the conductivity is  
 175 inversely proportional to  $\mathbf{V}$ , which means that the resistivity  $\rho$  is proportional to potential  $U(\theta)$ .  
 176 Similarly, the current  $I$  is proportional to  $U(\theta)$  because it is proportional to  $\mathbf{V}$ , and  $\mathbf{V}$  is  
 177 proportional to  $U(\theta)$ .

178 The relationship between radius  $R$  and circumferential potential  $U(\theta)$  can not be directly  
 179 seen from the formula. A hypothesis-verification method is used to confirm that  $R$  is inversely  
 180 proportional to the circumferential potential  $U(\theta)$ .

181 In order to avoid the influence of wavenumber selection on the calculation of potential  
 182 value, we employ the fitting formula to explicitly solve the inverse Fourier transform of the  
 183 wavenumber domain and derive the approximate analytical potential solution on the cross-section  
 184 where the point source is located. 201 wavenumbers are included in the fitting. Although the  
 185 computing time is relatively longer, the accuracy can be much higher.

186 The circumference potentials of two homogenous cylindrical models (Model 1 and Model  
 187 2) are calculated. The radius of Model 1 is 0.5m and the resistivity of Model 1 is  $600\Omega \cdot m$ . The  
 188 two current electrodes are placed on (0.5, 0) and (-0.5, 0), and their current intensities are -0.02A  
 189 and 0.02A respectively. The parameter setting of model 2 is the same as model 1 except that the  
 190 radius is set to be 0.3m. With  $U_1$  and  $U_2$  being the circumferential potential of model 1 and model

191 2 respectively, as are shown in figure 4, the ratios between  $U_1$  and  $U_2$  are almost equal to 1.667  
 192 except for the points around  $0^\circ$ ,  $90^\circ$ ,  $180^\circ$  and  $270^\circ$ , where the potential equals either zero or infinite,  
 193 making the ratio meaningless. Nevertheless, for the other points, the ratios stay quite stable at  
 194 1.667, which is precisely the same as the ratio between the radius of model 2 and model 1. To date,  
 195 all the models we have calculated satisfy this rule. Therefore, we confirm that the radius  $R$  is  
 196 inversely proportional to the circumferential potential  $U(\theta)$  for an infinitely long homogeneous  
 197 cylindrical model. This conclusion can be also seen in the paper of Weidelt and Weller (1997).



198

199

**Figure 4.** The ratio between  $U_2$  and  $U_1$ .

200

201

202

203

204

205

206

207

208

From the above numerical analysis, we can conclude that  $U = \frac{I\rho}{R} f_{\theta_{AB}}(\theta)$ .  $f_{\theta_{AB}}(\theta)$ , which we define as source function, is a function of  $\theta$  and its coefficients are determined only by  $\theta_{AB}$ . For a specific homogeneous cylinder, when given a certain  $\theta_{AB}$ ,  $V$  of a certain  $\lambda$  can be numerically calculated, thus the  $V$  is the function of  $\lambda$ . Nevertheless, they are discrete nodes. To overcome the discrete integration problem, we use the following process to calculate  $f_{\theta_{AB}}(\theta)$ . First of all, fitting the  $V(\lambda)$  with an elementary function. Secondly, applying function (4) to calculate the circumferential potential directly since the  $V(\lambda)$  is an elementary function after fitting. For better understanding, the circumferential potential calculated by this fitting method is denoted by  $U_{fit}(\theta)$ . Lastly, combining the analyses above,  $U_{fit}(\theta)$  equals to  $\frac{I\rho}{R} f_{\theta_{AB}}(\theta)$ . Then we acquire

$$f_{\theta_{AB}}(\theta) = \frac{R}{I \cdot \rho \cdot U_{fit}(\theta)} \quad (7)$$

209

210

211

It should be noted that for a certain  $\theta_{AB}$ , the  $f_{\theta_{AB}}(\theta)$  can be calculated and stored on a hard disk. Summarizing the results in the above sections we write the relationship between the circumferential potential of a cylindrical model and other parameters as

$$U(\theta) = \frac{I \cdot \rho}{R} f_{\theta_{AB}}(\theta) \quad (8)$$

212

213

214

215

We call the formulation (8) the approximate analytic solution of the circumferential potential distribution of an infinite homogeneous cylindrical model. This function can be used to modify the optimization wavenumber selection and calculate the geometric factor that are suitable for cylindrical objects.

216 2.3 The Modified Optimization Wavenumber Selection

217 Assume using  $n$  electrodes in the calculation, the included angle between current electrode  
 218 A and these nodes are  $\theta_1 \dots \theta_i \dots \theta_n$  and the corresponding coordinates are  $(x_1, z_1) \dots (x_i, z_i) \dots$   
 219  $(x_n, z_n)$ .  $m$  denotes the quantity of the total used wavenumbers. Combining equation (5) and  
 220 equation (8) we acquire

$$\frac{I \cdot \rho}{R} f_{\theta_{AB}}(\theta_i) = \sum_{j=1}^m V(x_i, \lambda_j, z_i) \cdot g_j \quad (9)$$

221 For an infinitely long homogeneous cylindrical model,

$$\sum_{j=1}^m V(x_i, \lambda_j, z_i) \cdot g_j \cdot R / [I \cdot \rho \cdot f_{\theta_{AB}}(\theta_i)] \approx 1 \quad (10)$$

222 The matrix form of equation (10) is

$$\mathbf{A} \mathbf{g} \approx \mathbf{L} \quad (11)$$

223 with the element of matrix  $\mathbf{A}$  ( $n \times m$  dimensions) being  $a_{ij} = R \cdot V(x_i, \lambda_j, z_i) / [I \cdot \rho \cdot f_{\theta_{AB}}(\theta_i)]$ , the  
 224 element of matrix  $\mathbf{g}$  ( $m \times 1$  dimensions) being  $g_j$  and  $\mathbf{L}$  being the  $n \times 1$  dimensional unit vector. By  
 225 incorporating the optimization wavenumber selection algorithm (Xu et al., 2000), the optimized  
 226 wavenumbers and the corresponding weighting coefficients can be calculated iteratively.

227 It should be noted that both  $\theta_{AB}$  and  $R$  could greatly influence the optimized wavenumber  
 228 series. To avoid the influence of  $R$ , we propose a new way named as the converting process to  
 229 avoid its influences basing on the fact that the radius  $R$  is inversely proportional to  $U(\theta)$  for a  
 230 cylindrical model. We only store the optimized wavenumber series when the radius equals a  
 231 standard value  $R_0$ . When the radius of the model in the real case equals  $R_1$ , we first enlarge the  
 232 discrete model linearly into cylinder  $R_0$ , apply the stored optimized wavenumber series to the  
 233 forward modeling process and then multiply the potential by  $R_0/R_1$ .

234 2.4. The Differential ERT Algorithm

235 Typically, the differential ERT uses the data sets collected before and after the resistivity  
 236 change to reconstruct the image. Set the model resistivity and the detected apparent resistivity  
 237 distribution at time  $t_1$  as  $\rho'$  and  $\rho'_s$  respectively. At time  $t_2$ , the resistivity and the detected apparent  
 238 resistivity distribution change into  $\rho''$  and  $\rho''_s$  respectively. Let  $\mathbf{x} = \log_e \rho'' - \log_e \rho'$  and  $\mathbf{z} =$   
 239  $\log_e \rho''_s - \log_e \rho'_s$  (Adler and Guardo, 1996). For small changes around a background resistivity  
 240 the relationship between  $\mathbf{x}$  and  $\mathbf{z}$  can be linearized as (Graham and Adler, 2006)

$$\mathbf{z} = \mathbf{J} \mathbf{x} + \mathbf{n} \quad (12)$$

241 where  $\mathbf{J}$  is the Jacobian matrix ( $m \times n$  dimensions,  $m$ : total measurements,  $n$ : total mesh grids) with  
 242 its element  $J_{ij} = \frac{\partial \log_e \rho_{si}}{\partial \log_e \rho_j}$  being  $\frac{\partial \log_e \rho_{si}}{\partial \log_e \rho_j}$ .  $\rho_{si}$  denotes the apparent resistivity during the  $i$ -th data  
 243 collection and  $\rho_j$  denotes the model resistivity on the  $j$ -th mesh.  $\mathbf{n}$  denotes the noise matrix. In  
 244 order to overcome the ill-conditioning of  $\mathbf{J}$  we solve (12) using the following regularized inverse  
 245 (Graham and Adler, 2006):

$$\mathbf{x} = (\mathbf{J}^T \mathbf{W} \mathbf{J} + \beta \mathbf{R})^{-1} \mathbf{J}^T \mathbf{W} \mathbf{z} = \mathbf{B} \mathbf{z} \quad (13)$$

246 where  $\mathbf{R}$  is a regularization matrix,  $\beta$  is a scalar hyperparameter (Batu and Çetin, 2008; Braun et  
 247 al., 2017; Graham and Adler, 2006) that controls the amount of regularization and  $\mathbf{W}$  is a  $m \times m$   
 248 dimensional diagonal matrix with its diagonal element  $W_{ii}$  being  $1/\eta_i^2$ .  $\eta_i^2$  is the noise variance  
 249 of the  $i$ -th data collection. Usually there are three ways to calculate  $\mathbf{R}$ . (1)  $\mathbf{R} = \mathbf{I}$ , making equation  
 250 (13) the 0-th order Tikhonov algorithm. (2)  $\mathbf{R} = \text{diag}(\mathbf{H}^T \mathbf{H})$ , making equation (13) the  
 251 regularization matrix used in the NOSER algorithm (Cheney et al., 2010), (3)  $\mathbf{R}$  is modeled as a  
 252 spatially invariant Gaussian high pass filter (Adler and Guardo, 1996).

### 253 3. Experimental Experiments

#### 254 3.1. The Apparent Resistivity Tomography for the Cylindrical Object

255 By employing the modified optimization wavenumbers in the 2.5-dimensional resistivity forward  
 256 modeling, we can obtain the potential distribution of the cylinder cross-section. The process of  
 257 converting the potential into apparent resistivity should also be adapted accordingly because this  
 258 is also based on the analytic solution of the detected objects. The key to calculate the apparent  
 259 resistivity is the geometric factor  $G$ . In analogy with the geometric factor calculation of half-space,  
 260 we propose an algorithm to calculate the geometric factor of cylindrical models. Name the two  
 261 receivers as M and N and the corresponding potentials of the cylinder model are  $U_M$  and  $U_N$   
 262 respectively. Then we acquire

$$U_M = \frac{I \cdot \rho}{R} f_{\theta_{AB}}(\theta_M) \quad (14)$$

$$U_N = \frac{I \cdot \rho}{R} f_{\theta_{AB}}(\theta_N) \quad (15)$$

263 where  $\theta_M$  and  $\theta_N$  stand for their locations on the circumferential surface. The potential difference  
 264 between M and N is

$$\Delta U_{MN} = \frac{I\rho}{R} [f_{\theta_{AB}}(\theta_M) - f_{\theta_{AB}}(\theta_N)] \quad (16)$$

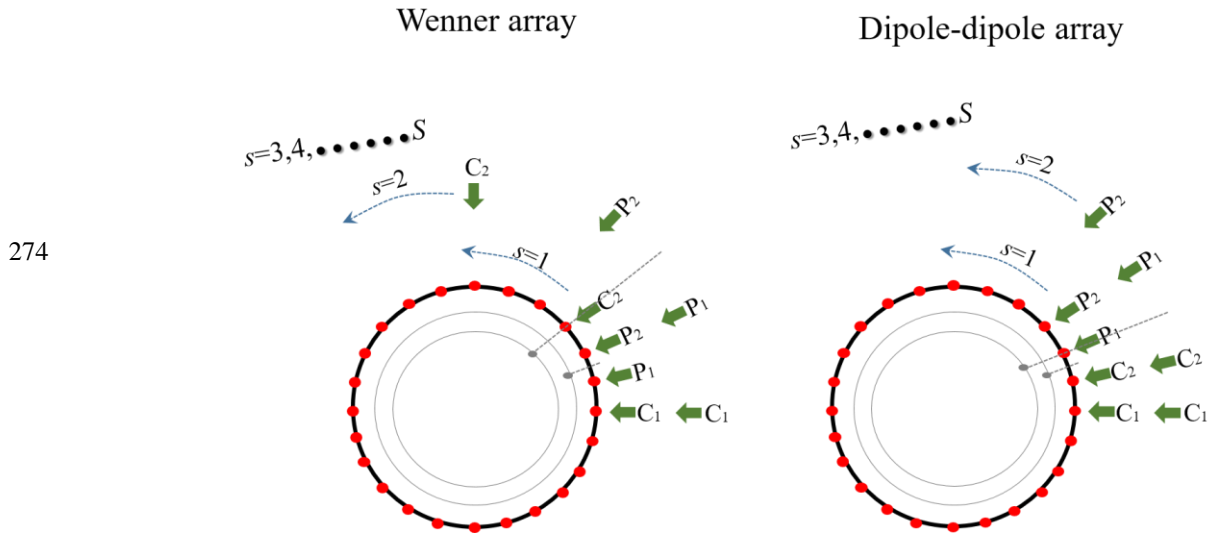
265 Rewrite equation (16) as

$$\rho = \frac{\Delta U_{MN} \cdot R}{I \cdot [f_{\theta_{AB}}(\theta_M) - f_{\theta_{AB}}(\theta_N)]} \quad (17)$$

266 Then the geometric factor of the cylindrical model should be:

$$G = \frac{R}{f_{\theta_{AB}}(\theta_M) - f_{\theta_{AB}}(\theta_N)} \quad (18)$$

267 Using the geometric factors introduced above, we conduct the forward modeling of three models  
 268 using the Wenner and dipole-dipole array. Figure 5 shows these two kinds of electrode  
 269 arrangements.  $C_1$  and  $C_2$  stand for the two current electrodes,  $P_1$  and  $P_2$  stand for the two receivers,  
 270  $a$  and  $s$  are the electrode spacing and number,  $S$  is the total detected layer and  $t$  is the total electrodes.  
 271 For the Wenner array, the equally spaced  $C_1$ - $P_1$ - $P_2$ - $C_2$  moves one by one and detects  $t$  times in each  
 272 layer. For dipole-dipole array,  $C_1$ - $C_2$  and  $P_1$ - $P_2$  remain as  $a$ ,  $C_2$ - $P_1$  equals to  $s \times a$  and still detect  $t$   
 273 times in each layer.

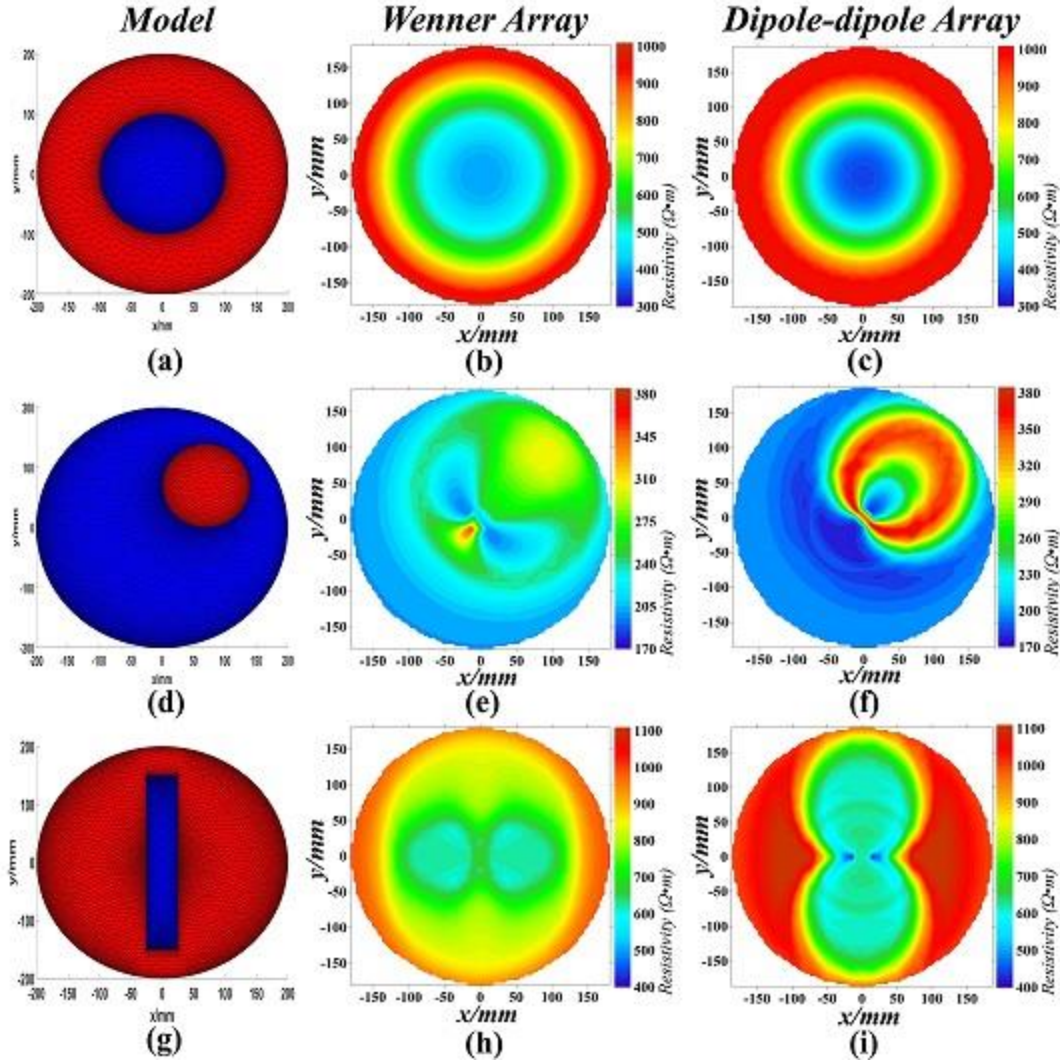


274

275

**Figure 5.** Wenner array and dipole-dipole array.

276 Figure 6 shows the calculated apparent resistivity results of three kinds of models. Thirty-two  
 277 electrodes are employed and the radius is 0.2m. Compared with Wenner array, the dipole-dipole  
 278 array has a higher contrast, which means that it is more sensitive to both anomaly and noise. When  
 279 the anomaly locates in the central, the two apparent resistivity contour maps may be able to show  
 280 its location, but when the anomalies locate otherwise or have a complex shape, the apparent  
 281 resistivity distributions are not enough to recognize the anomaly. In some cases, the apparent  
 282 resistivity distribution of the Wenner array is totally contrary to the results of dipole-dipole array  
 283 because of the different location of the electrodes. The apparent resistivity can indeed reveal parts  
 284 of the information in the cylindrical bodies, especially when there are no anomalies or the  
 285 anomalies are located in the central. However, it is somehow limited for the analysis of  
 286 complicated objects. For better application of ERT, more works need to be done to reconstruct the  
 287 resistivity distribution.



288

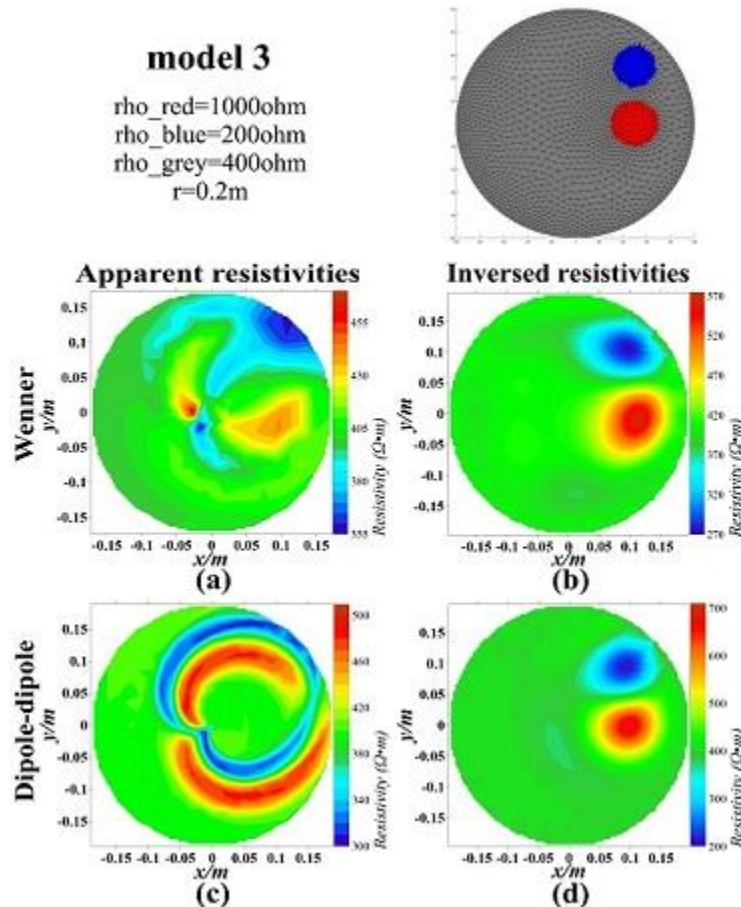
289 **Figure 6.** Apparent resistivity ( $\Omega \cdot m$ ) calculation results of three different models. First column:  
 290 (a), (d) and (g) are three different models with unstructured meshes, the red part is  $1000 \Omega \cdot m$  and  
 291 the blue part is  $200 \Omega \cdot m$ . Second column: (b), (e) and (h) are the apparent resistivity distributions  
 292 of (a), (d) and (g) respectively using the Wenner array. Third column: (c), (f) and (i) are the  
 293 apparent resistivity distributions of (a), (d) and (g) respectively using the dipole-dipole array.

### 294 3.2. The differential ERT of the synthetic data

295 We use the differential ERT mentioned in section 2.4 to retrieve the resistivity distribution of  
 296 model 3 (Figure. 7) from the forward modeling result. As is shown in figure 7, model 3 is a cylinder  
 297 with two anomalies located on edge, and its radius is 0.2m. The resistivities in the red, blue, and  
 298 grey part are  $1000 \Omega \cdot m$ ,  $200 \Omega \cdot m$  and  $400 \Omega \cdot m$  respectively. Twenty-four electrodes are employed.  
 299 The total detected layers for the Wenner and dipole-dipole array are seven and twenty-one. During  
 300 the inversion,  $\eta_i^2 = 700$ ,  $\mathbf{R} = \text{diag}(\mathbf{H}^T \mathbf{H})$  and  $\beta = 0.016$ . The model detected in  $t_1$  is set as a  
 301 homogenous cylindrical model.

302 Figure 7 displays the parameters and unstructured meshes of model 3 in the first row. The second  
 303 row introduces the Wenner array forward (left) and inversion (right) results and the third row

304 displays dipole-dipole array forward (left) and inversion (right) results. The reconstructed images  
 305 of both the Wenner array and dipole-dipole array show high resolutions of the two adjacent  
 306 anomalies and the inversion processes of both arrays only take about 3.67 seconds on a  
 307 computer(Intel(R) Core(TM) i3-2100 CPU @ 3.10GHz RAM 16GB) since the Jacobian matrix  
 308 can be calculated in advance and stored on the hard disk.



309

310 **Figure 7.** Apparent resistivity ( $\Omega \cdot m$ ) distributions of model 3 and their inversed resistivity  
 311 distributions. (a): Apparent resistivity distributions of model 3 using the Wenner array. (b):  
 312 Inversed resistivity distributions of (a) using the differential ERT. (c) Apparent resistivity  
 313 distributions of model 3 by the dipole-dipole array. (d) Inversed resistivity distributions of (c) by  
 314 the differential ERT.

## 315 4. Experimental Results and Analysis

### 316 4.1. Experimental Set-up

317 For experimental model preparation, four steps are included. (1) Making the cylinder tube tank:  
 318 Prepare a cylinder PVC tube of radius 99.75mm and height 1 m with the bottom glued with a  
 319 plastic board. Punch equidistantly twenty-four holes of radius about 2mm on the circumference of  
 320 height 0.5m. (2) Handcrafting the microelectrode: To decrease as much as possible the influence  
 321 of the electrodes, we need to keep the radius as small as possible. Cut the multi-strand copper wire  
 322 into 2cm long and peel off the rubber. Each copper thread can be used as a microelectrode. The

323 radius of our microelectrodes is less than 0.5mm. Inserting these microelectrodes into the holes of  
 324 the tube one by one and seal the hole with glue. (3) Preparing the conductive water: Add 2.85g  
 325 sodium chloride (NaCl) crystal to 30L distilled water. The average resistivity of this NaCl solution  
 326 is  $36.56\Omega\cdot\text{m}$  after several measurements. Pour the conductive water into the cylindrical tube model.  
 327 (4) Simulating the anomaly: We put a homogenous rubber bar of radius 36.485mm and height  
 328 1.08m into the cylinder tank. Its average resistivity is estimated at  $250\Omega\cdot\text{m}$  after several detections.  
 329 After model preparation, we use the DUK-2B Multi-Electrode Resistivity Survey System (CGE  
 330 (Chongqing) Geological Instrument Co., Ltd) for data collection and artificially transfer the  
 331 electrode. Figure 8 shows the detections of the two models in the lab. Model 4 is a homogenous  
 332 cylinder filled with NaCl solution and model 5 has a rubber bar as an anomaly standing in the  
 333 center.



Figure 8. The detection process.

334

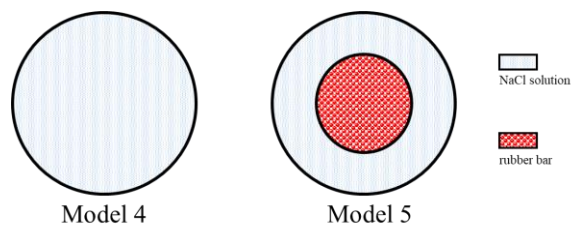
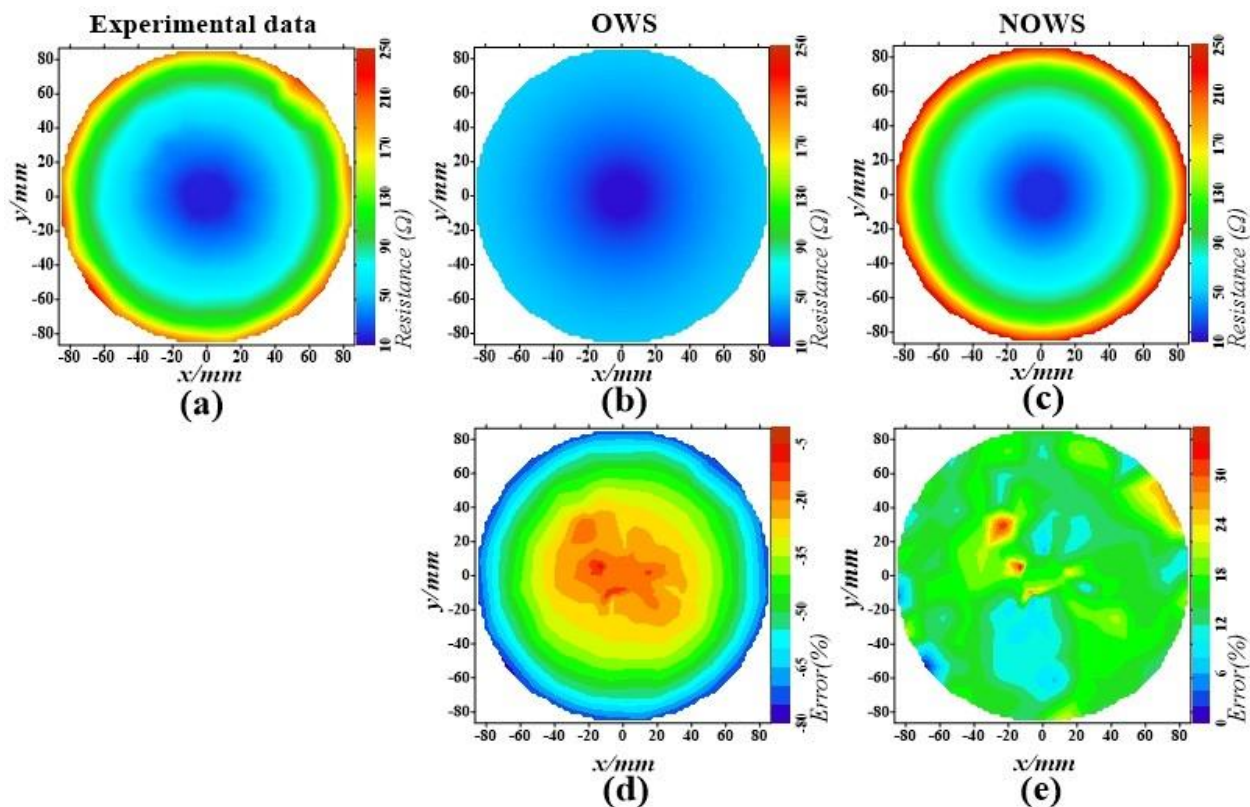


Figure 9. The cross sections of model 4 and model 5 in lab.

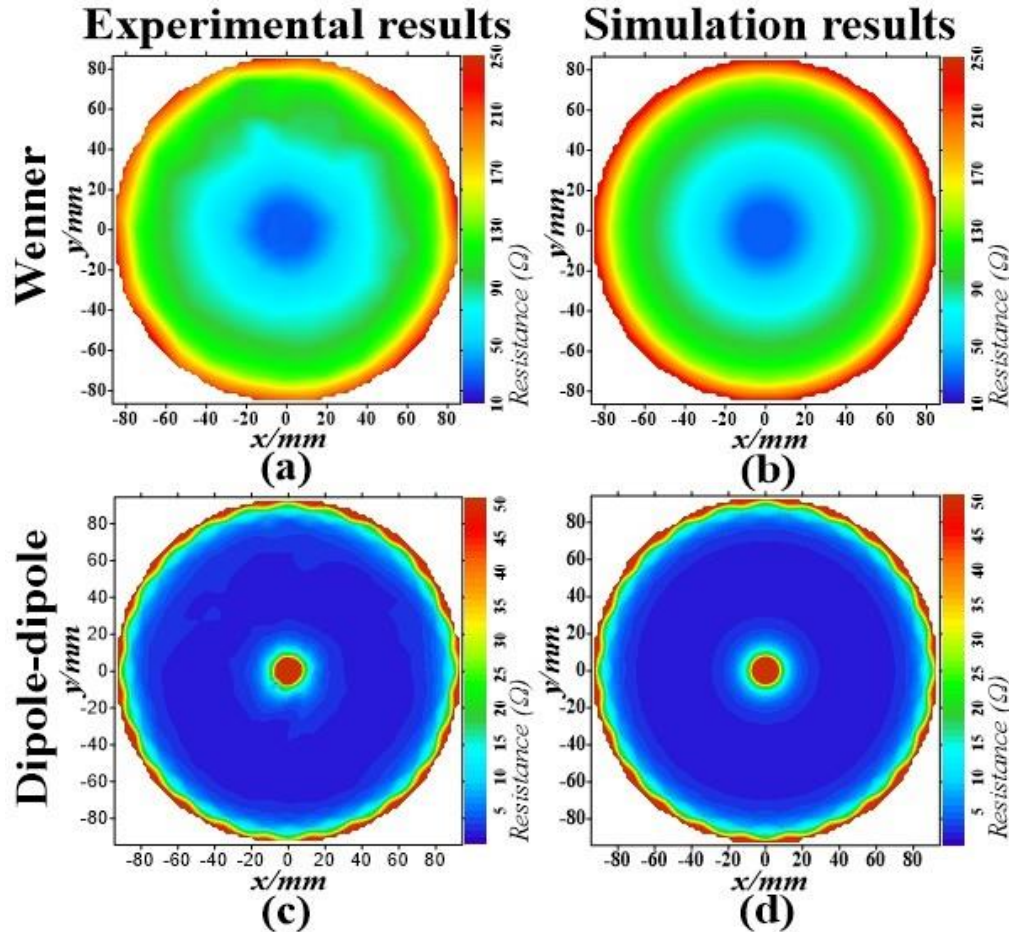
#### 335 4.2. Experimental Results

336 To compare the accuracy of the forward modeling results using different kinds of wavenumbers,  
 337 the resistance:  $U/I$  of both experimental results and numerical modeling results are calculated. For  
 338 the numerical calculation, the other parameters are set the same with the laboratory model except  
 339 for the wavenumbers in order to highlight its affection on accuracy. The difference between  
 340 simulated resistance  $r_s$  and the experimental resistance  $r_e$  is calculated using  $(r_s - r_e)/r_e$ . As is shown

341 in figure 10, the difference between the experimental resistance and the simulated resistance when  
 342 using the traditional optimization wavenumbers ranges from -80% to -5%. The closer to the surface,  
 343 the greater the difference can be. Nevertheless, when using the modified optimization  
 344 wavenumbers, the difference ranges from 0% to 18% with few points reaching 34% randomly  
 345 occurring because of the noise of the experimental data. Comparing the two kinds of simulated  
 346 resistance data, we can easily draw the conclusion that the modified optimization wavenumbers  
 347 can significantly reduce the error for 2.5-dimensional resistivity forward modeling of cylindrical  
 348 objects. Although there are still some differences between the experimental data and the simulated  
 349 data using the modified optimization wavenumbers, the simulation is not the only one to be  
 350 responsible for that because the experimental data can be affected by many other factors. The fact  
 351 that the modified optimization wavenumbers can achieve better 2.5-dimensional resistivity  
 352 forward modeling results of cylindrical models is not a coincidence because this is also true for  
 353 model 5. Figure 11 displays the simulated resistance distribution of both the Wenner and dipole-  
 354 dipole array of model 5. The simulation results match pretty well with the experimental data.  
 355



357 **Figure 10.** The experimental and simulated resistance ( $\Omega$ ) distribution of model 4 and their  
 358 differences (%). (a) The experimental resistance distribution. (b) The simulated resistance  
 359 distribution using the traditional optimization wavenumbers. (c) The simulated resistance  
 360 distribution using the modified optimization wavenumbers. (d) The difference between the  
 361 experimental resistance and the simulated resistance when using the traditional optimization  
 362 wavenumbers. (e) The difference between the experimental resistance and the simulated resistance  
 363 when using the modified optimization wavenumbers.



364

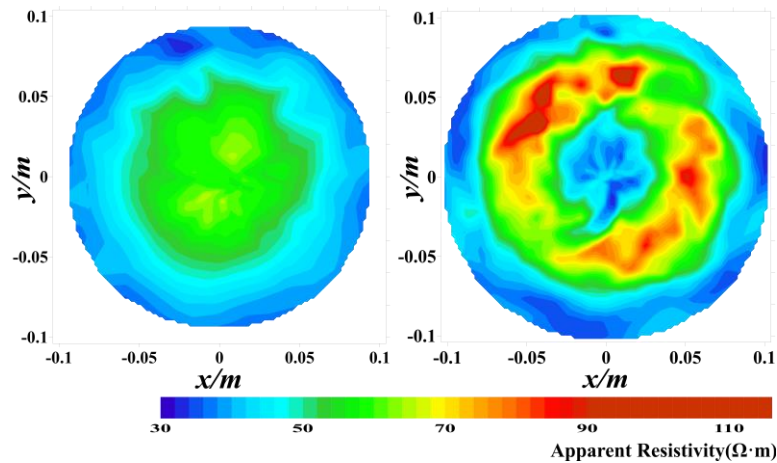
365 **Figure 11.** The experimental and simulated resistance ( $\Omega$ ) distribution of model 5. (a) The  
 366 experimental resistance distribution using the Wenner array. (b) The simulated resistance  
 367 distribution using the Wenner array. (c) The experimental resistance distribution using the dipole-  
 368 dipole array. (d) The simulated resistance distribution using the dipole-dipole array.

369 To test the performance of the differential ERT method on the lab data, the experimental result of  
 370 model 5 is employed in the calculation. During the image reconstruction,  $\mathbf{R} = \text{diag}(\mathbf{H}^T \mathbf{H})$ ,  $\eta_i^2 =$   
 371 700 and  $\beta=0.016$ . The inversion results are shown in figure 12.

372 Though the inversion processes do not include the removal of bad points, the reconstructed images  
 373 still match well with the real model. The inversions are done immediately since the Jacobian matrix  
 374 is calculated and stored on a hard disk. This is to say that the differential ERT has the advantages  
 375 of both time-saving and high anti-interference ability. When comparing the reconstructed images  
 376 of the Wenner array and dipole-dipole array, we can see directly that the results of the dipole-  
 377 dipole array have higher contrast. The total independent measuring points of the dipole-dipole  
 378 array are more than those of the Wenner array, increasing its certainty greatly. Unlike in the half-  
 379 space ground condition, the dipole-dipole array is less affected by electrode distance in cylindrical  
 380 objects due to the relatively small detection area. The more independent measurements we take,  
 381 the more accurate the inversion results will be. Therefore in the case of applying a certain number  
 382 of electrodes, making as many independent measurements as possible in cylinder detection is an  
 383 essential idea in designing electrode arrangements.

384

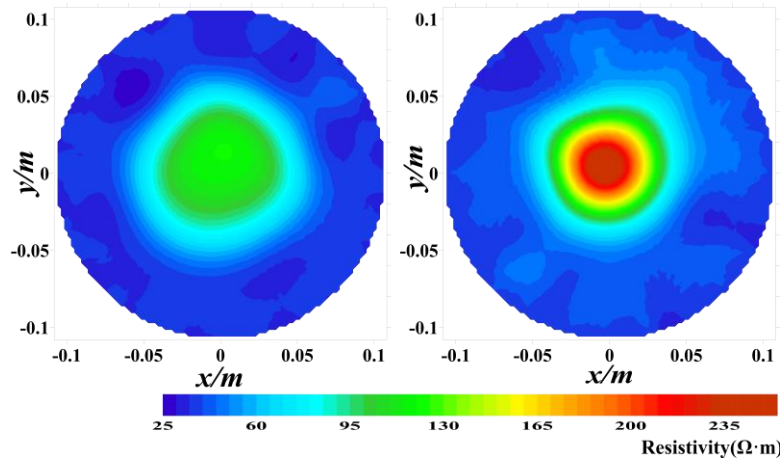
385



386

(a)

387



388

(b)

389 **Figure 12.** Inversion results of model 5 by the differential ERT. (a) The experimental apparent  
 390 resistivity distribution by the Wenner array (left) and the Inversed resistivity distribution (right).  
 391 (b) The experimental apparent resistivity distribution by the dipole-dipole array (left) and the  
 392 inversed resistivity distribution (right).

## 393 5. Discussions

394 For decades, massive researches have proved that the ERT method performs pretty well in  
 395 identifying low-resistivity (or high-resistivity) anomalies in the shallow half-surface. The  
 396 numerical modeling and inversion algorithm together with the experiment described in this paper  
 397 illustrate that the ERT can also be well applied to determine contrast resistivity anomalies of a  
 398 cylindrical object. Thus enabling the ERT method to be applied to more areas such as tree trunk  
 399 imaging for environmental protection, defect detection in construction materials, lung imaging for  
 400 medical science, etc. However, there are several issues that still need to be addressed: the selection  
 401 of hyperparameter in time difference imaging, the array arrangements, etc. Our next interest, for  
 402 numerical imaging, is to study the high order differential ERT, and for in situ application is to  
 403 propose a more suitable array arrangement and finally lead to better applications.

404 For the inversion part, the hyperparameter in this paper is chosen as 0.016 directly from an  
 405 empirical point of view. Graham and Adler (2006) introduced five ways to objectively select  
 406 hyperparameters. But for specific survey issues, the corresponding hyperparameter selection may  
 407 need more specific discussions. The inversion results of model 3 in figure 7 show high resolutions  
 408 of the two adjacent anomalies, however, two problems still remain. Firstly, their true resistivities  
 409 are not revealed well. That's because the differential ERT method we use is a one-order linearized  
 410 approximation. To achieve both high resolutions and true resistivity reconstructions, the high order  
 411 image construction (Chan et al., 2000; Jiang et al., 2014) is suggested to be carefully studied and  
 412 introduced into the geophysical inversion. Secondly, there are regular noises near the electrodes in  
 413 the inversion results. These are also regular in other papers (D. Bieker et al., 2010; Bieker and  
 414 Rust, 2010; Wang et al., 2016), we think that the main cause is that the potential around the current  
 415 nodes are complicated and can't be perfectly matched with the fitted values. There are mainly two  
 416 kinds of ways to solve this problem. One is to increase the accuracy of the approximate analytic  
 417 solution of the infinitely long homogeneous cylindrical model and the other is to place the receivers  
 418 far from the current nodes.

419 Vauhkonen et al. (1999) described that it is yet not clear to which task one should direct the effort,  
 420 for example, the increase of the number of electrodes, estimation of feasible conditions for the  
 421 termination boundary or the accuracy of the geometrical modeling of the object boundary. Well,  
 422 in this paper we might have the answer. First, theoretically, the increasing number of electrodes  
 423 does increase the accuracy of image reconstruction since it brings more information. Nevertheless,  
 424 the number of electrodes we use should depend on the detection precision required. Second, the  
 425 geometrical modeling of the object boundary does have a great influence on the forward modeling  
 426 results. In our numerical analysis, the effect of boundary geometry is transferred into the effect of  
 427 wavenumber selections on the forward modeling results. The error caused by wrongly selected  
 428 wavenumbers, or wrongly described boundary geometry, can reach as many as 80%. Therefore,  
 429 both the number of electrodes and the boundary conditions should be studied seriously.

## 430 **6. Conclusions**

431 For an infinitely long homogeneous cylindrical model, we summarize its circumferential potential  
 432 distribution as  $U(\theta) = \frac{I \cdot \rho}{R} f_{\theta AB}(\theta)$ . Thus the circumferential potential  $U(\theta)$  is inversely  
 433 proportional to the radius  $R$  and proportional to the current intensity  $I$ , the resistivity  $\rho$  and the  
 434 source function  $f_{\theta AB}(\theta)$ .  $f_{\theta AB}(\theta)$  is a function of  $\theta$  and its coefficients are determined only by the  
 435 included angle between two current electrodes. This relationship is easy but very significant  
 436 because it is the basis of many other numerical approximations and no other papers have proposed  
 437 this as far as we know. Basing on this newly proposed approximate analytic solution for the  
 438 infinitely long homogeneous cylindrical model, the modified optimization wavenumber selection  
 439 is derived, which is used for selecting wavenumbers for 2.5-dimensional resistivity modeling of  
 440 cylindrical objects. The core idea of this adaption is to replace the analytic solutions of half-space  
 441 ground with the approximate analytic solution of the infinitely long homogeneous cylindrical  
 442 model. Both numerical results and experimental results have proved that it can greatly improve  
 443 the accuracy of 2.5-dimensional forward modeling of cylinder objects.

444 In order to erase the effect of radius on wavenumber selection, which means preventing from  
 445 selecting the optimized wavenumbers every time, we need to include the converting process in the  
 446 computing process. The concept is to model the cylinder in a unified radius firstly and then convert  
 447 the potential to the actual value basing on the fact that the potential is inversely proportional to the

448 radius. The apparent resistivity of cylindrical models can be pretty different due to their special  
449 geometry. Basing on the approximate analytic solution for the infinitely long homogeneous  
450 cylindrical model, we presented the geometric factor calculation method for apparent resistivity  
451 tomography of cylindrical objects in analogy with the geometric factor calculation of half-space.

452 By incorporating all these new concepts in numerical simulation, we present the resistivity  
453 reconstruction method for cylindrical objects. It is timesaving, cost-effective and has good anti-  
454 interference capacity. The experimental results correlate pretty well with the numerical modeling  
455 results, furtherly verifying that the modified optimization wavenumbers can result in better  
456 accuracy than the traditional optimization wavenumbers and the proposed 2.5-dimensional fast  
457 resistivity reconstruction scheme has great promise for cylindrical object imaging.

## 458 Acknowledgments

459 This work was supported in part by the Project of the State Key Research and Development Plan  
460 under Grant No. 2018YFE0208300, in part by the National Natural Science Foundation of China  
461 under Grant No. 41874084, U2039206, and in part by the Anhui Natural Science Foundation  
462 under Grant 2008085QD176.

## 463 References

- 464 Adler A. & Guardo R., 1996 Electrical impedance tomography: regularized imaging and contrast detection.  
465 *IEEE Transactions on Medical Imaging*, 15(2), 170-179. <https://doi.org/10.1109/42.491418>
- 466 Apostolopoulos G., 2008. Combined Schlumberger and dipole-dipole array for hydrogeologic  
467 applications. *Geophysics*, 73(5), F189-F195. <https://doi.org/10.1190/1.2950032>
- 468 Augusto M. C., Innocenti H. L. P., Paulo N. & Melo I. L., 2017. Analysis of leaks from  
469 geomembrane in a sanitary landfill through models of electrical resistivity tomography in  
470 South Brazil. *Environmental Earth Sciences*, 77(1), 7. <https://doi.org/10.1007/s12665-017-7180-x>
- 471 Batu Ö. & Çetin M., 2008. Hyper-parameter selection in non-quadratic regularization-based radar  
472 image formation. *Proceedings of SPIE - The International Society for Optical Engineering*,  
473 6970. <https://doi.org/10.1117/12.782341>
- 474 Bieker, Dirk, Rust & Steffen, 2010. Electric resistivity tomography shows radial variation of  
475 electrolytes in *Quercus robur*. *Canadian Journal of Forest Research*. 40,1189-1193.  
476 <https://doi.org/10.1139/X10-076>
- 477 Bieker D., Kehr R., Weber G. & Rust S., 2010. Non-destructive monitoring of early stages of white  
478 rot by *Trametes versicolor* in *Fraxinus excelsior*. *Annals of Forest Science*, 67(2), 210-210.  
479 <https://doi.org/10.1051/forest/2009103>
- 480 Bieker D. & Rust S., 2010. Non-destructive estimation of sapwood and heartwood width in Scots  
481 pine (*Pinus sylvestris* L.). *Silva Fennica*, 44(2), 267-273. <https://doi.org/10.14214/sf.153>
- 482 Braun F., Proenca M., Sola J., Thiran J.-P. & Adler A., 2017. A Versatile Noise Performance  
483 Metric for Electrical Impedance Tomography Algorithms. *IEEE Transactions on*  
484 *Biomedical Engineering*, 64(10), 2321-2330. <https://doi.org/10.1109/tbme.2017.2659540>
- 485

- 486 Brazey B., Haddab Y. & Zemiti N., 2022. Robust imaging using electrical impedance tomography:  
487 review of current tools. *Proceedings of the Royal Society a-Mathematical Physical and*  
488 *Engineering Sciences*, 478(2258). <https://doi.org/10.1098/rspa.2021.0713>
- 489 Cao L., Li H., Fu D., Liu X. & Fu F., 2020. Real-time imaging of infarction deterioration after  
490 ischemic stroke in rats using electrical impedance tomography. *Physiological*  
491 *Measurement*, 41(1), 015004. <https://doi.org/10.1088/1361-6579/ab69ba>
- 492 Chan T., Marquina A. & Mulet P., 2000. High-Order Total Variation-Based Image Restoration.  
493 *SIAM Journal on Scientific Computing*, 22(2), 503-516.  
494 <https://doi.org/10.1137/s1064827598344169>
- 495 Cheney M., Isaacson D., Newell J. C., Simske S. & Goble J., 2010. NOSER: An algorithm for  
496 solving the inverse conductivity problem. *International Journal of Imaging Systems &*  
497 *Technology*, 2(2), 66-75. <https://doi.org/10.1002/ima.1850020203>
- 498 Coggon J. H., 1971. Electromagnetic and Electrical Modeling by the Finite Element Method.  
499 *Geophysics*, 36(1), 132-155. <https://doi.org/10.1190/1.1440151>
- 500 Coscia I., Linde N., Greenhalgh S., Vogt T. & Green A., 2012. Estimating traveltimes and  
501 groundwater flow patterns using 3D time-lapse crosshole ERT imaging of electrical  
502 resistivity fluctuations induced by infiltrating river water. *Geophysics*, 77(4), E239-E250.  
503 <https://doi.org/10.1190/Geo2011-0328.1>
- 504 Dumont G., Robert T. & Nguyen F., 2018. Electrical resistivity tomography and distributed  
505 temperature sensing monitoring to assess the efficiency of horizontal recirculation drains  
506 on retrofit bioreactor landfills. *Geophysics*, 83(2), B13-B23.  
507 <https://doi.org/10.1190/Geo2016-0622.1>
- 508 Elliott M. L., Broschat T. K. & Göcke L., 2016. Preliminary Evaluation of Electrical Resistance  
509 Tomography for Imaging Palm Trunks. *Arboriculture & Urban Forestry*, 42(2), 111-119.  
510 <https://doi.org/10.48044/jauf.2016.010>
- 511 Franco R. d., Biella G., Tosi L., Teatini P., Lozej A., Chiozzotto B., . . . Gasparetto-Stori G., 2009.  
512 Monitoring the saltwater intrusion by time lapse electrical resistivity tomography: The  
513 Chioggia test site (Venice Lagoon, Italy). *Journal of Applied Geophysics*, 69(3-4), 117-  
514 130. <https://doi.org/10.1016/j.jappgeo.2009.08.004>
- 515 Gao J., Smirnov M., Smirnova M. & Egbert G., 2020. 3-D DC Resistivity Forward Modeling  
516 Using the Multi-resolution Grid. *Pure and Applied Geophysics*, 177(4), 1-17.  
517 <https://doi.org/10.1007/s00024-019-02365-3>
- 518 Graham B. M. & Adler A., 2006. Objective selection of hyperparameter for EIT. *Physiol Meas*,  
519 27(5), S65-79. <https://doi.org/10.1088/0967-3334/27/5/S06>
- 520 Günther T., Rücker C. & Spitzer K., 2006. Three-dimensional modelling and inversion of DC  
521 resistivity data incorporating topography – II. Inversion. *Geophysical Journal of the Royal*  
522 *Astronomical Society*, 166(2), 506-517. [https://doi.org/10.1111/j.1365-](https://doi.org/10.1111/j.1365-246X.2006.03011.x)  
523 [246X.2006.03011.x](https://doi.org/10.1111/j.1365-246X.2006.03011.x)
- 524 Guyot A., Ostergaard K. T., Lenkopane M., Fan J. & Lockington D. A., 2013. Using electrical  
525 resistivity tomography to differentiate sapwood from heartwood: application to conifers.  
526 *Tree Physiology*, 33(2), 187-194. <https://doi.org/10.1093/treephys/tps128>
- 527 Hermans T., Vandenbohede A., Lebbe L. & Nguyen F., 2012. A shallow geothermal experiment  
528 in a sandy aquifer monitored using electric resistivity tomography. *Geophysics*, 77(1), B11-  
529 B21. <https://doi.org/10.1190/geo2011-0199.1>
- 530 Jiang L., Huang J., Lv X.-G. & Liu J., 2014. High-Order Total Variation-Based Image Restoration  
531 with Spatially Adapted Parameter Selection. *Proceedings of International Conference on*

- 532 *Computer Science and Information Technology (Csait 2013)*, 255, 67-74.  
533 [https://doi.org/10.1007/978-81-322-1759-6\\_9](https://doi.org/10.1007/978-81-322-1759-6_9)
- 534 Karhunen K., Seppänen A., Lehtikoinen A., Monteiro P. J. M. & Kaipio J. P., 2010. Electrical  
535 Resistance Tomography imaging of concrete. *Cement and Concrete Research*, 40(1), 137-  
536 145. <https://doi.org/10.1016/j.cemconres.2009.08.023>
- 537 Kazakis N., Pavlou A., Vargemezis G., Voudouris K. S., Soulios G., Pliakas F. & Tsokas G., 2016.  
538 Seawater intrusion mapping using electrical resistivity tomography and hydrochemical  
539 data. An application in the coastal area of eastern Thermaikos Gulf, Greece. *Sci Total*  
540 *Environ*, 543(Pt A), 373-387. <https://doi.org/10.1016/j.scitotenv.2015.11.041>
- 541 Lesparre N., Robert T., Nguyen F., Boyle A. & Hermans T., 2019. 4D electrical resistivity  
542 tomography (ERT) for aquifer thermal energy storage monitoring. *Geothermics*, 77, 368-  
543 382. <https://doi.org/10.1016/j.geothermics.2018.10.011>
- 544 Loke M. H. & Barker R. D., 1996. Rapid least - squares inversion of apparent resistivity  
545 pseudosections by a quasi - Newton method. *Geophysical Prospecting*, 44(1), 131-152.  
546 <https://doi.org/10.1111/j.1365-2478.1996.tb00142.x>
- 547 Losso A., Sailer J., Br A., Ganthaler A. & Mayr S., 2020. Insights into trunks of *Pinus cembra* L.:  
548 analyses of hydraulics via electrical resistivity tomography. *Trees*. <https://doi.org/10.1007/s00468-020-01976-x>
- 549
- 550 Mukanova B. M. I., 2018. The Boundary Element Method in the Sounding of Media with Ground  
551 Surface Relief. 115-152. <https://doi.org/10.1007/978-3-319-72908-4>
- 552 Persson P.-O. & Strang G., 2004. A Simple Mesh Generator in Matlab. *SIAM Review*, 46(2), 329-  
553 345. <https://doi.org/10.2307/20453511>
- 554 Rao G. R., Sattar M. A., Wajman R. & Jackowska-Strumillo L., 2021. Quantitative Evaluations  
555 with 2d Electrical Resistance Tomography in the Low-Conductivity Solutions Using 3d-  
556 Printed Phantoms and Sucrose Crystal Agglomerate Assessments. *Sensors*, 21(2), 1-31.  
557 <https://doi.org/10.3390/s21020564>
- 558 Ren H., Tian K., Hong S., Dong B., Xing F. & Qin L., 2019. Visualized investigation of defect in  
559 cementitious materials with electrical resistance tomography. *Construction and Building*  
560 *Materials*, 196(2019), 428-436. <https://doi.org/10.1016/j.conbuildmat.2018.11.129>
- 561 Ren Z., Kowalski A. & Rodgers T. L., 2017. Measuring inline velocity profile of shampoo by  
562 electrical resistance tomography (ERT). *Flow Measurement and Instrumentation*,  
563 58(2017), 31-37. <https://doi.org/10.1016/j.flowmeasinst.2017.09.013>
- 564 Ren Zhengrong T. J., 2010. 3D direct current resistivity modeling with unstructured mesh by  
565 adaptive finite-element method. *Geophysics*, 75(1), H7. <https://doi.org/10.1190/1.3298690>
- 566 Rucker C., Günther T. & Spitzer K., 2006. Three-dimensional modelling and inversion of DC  
567 resistivity data incorporating topography I: Modelling. *Geophysical Journal International*,  
568 166(2), 495-505. <https://doi.org/10.1111/j.1365-246X.2006.03010.x>
- 569 Sapkota A., Fuse T., Seki M., Maruyama O., Sugawara M. & Takei M., 2015. Application of  
570 electrical resistance tomography for thrombus visualization in blood. *Flow Measurement*  
571 *and Instrumentation*, 46(2015), 334-340.  
572 <https://doi.org/10.1016/j.flowmeasinst.2015.06.023>
- 573 Sardeshpande M. V., Kumar G., Aditya T. & Ranade V. V., 2016. Mixing studies in unbaffled  
574 stirred tank reactor using electrical resistance tomography. *Flow Measurement and*  
575 *Instrumentation*, 47(2016), 110-121. <https://doi.org/10.1016/j.flowmeasinst.2016.01.003>

- 576 Thanh N. D., Cho G. C., Sim Y. J. & Lee S. W., 2006. Evaluation of Grouting Performance Using  
577 Electrical Resistivity Tomography. *Key Engineering Materials*, 321-323, 1407-1410.  
578 <https://doi.org/10.4028/www.scientific.net/KEM.321-323.1407>
- 579 Tsili W., Sheng F. & Mezzatesta A. G., 2000. Three-dimensional finite-difference resistivity  
580 modeling using an upgridding method. *IEEE Transactions on Geoscience and Remote*  
581 *Sensing*, 38(4), 1544-1550. <https://doi.org/10.1109/36.851954>
- 582 Vauhkonen P. J., Vauhkonen M., Savolainen T. & Kaipio J. P., 1999. Three-dimensional electrical  
583 impedance tomography based on the complete electrode model. *IEEE Transactions on*  
584 *Biomedical Engineering*, 46(9), 1150-1160. <https://doi.org/10.1109/10.784147>
- 585 Wang H., Guan H., Guyot A., Simmons C. T. & Lockington D. A., 2016. Quantifying sapwood  
586 width for three Australian native species using electrical resistivity tomography.  
587 *Ecohydrology*, 9(1), 83-92. <https://doi.org/10.1002/eco.1612>
- 588 Weidelt P. & Weller A., 1997. Computation of geoelectrical configuration factor for cylindrical  
589 core samples. *Scientific Drilling*, 6(1), 27-34. <https://doi.org/>
- 590 Wu X., 2003. A 3-D finite-element algorithm for DC resistivity modelling using the shifted  
591 incomplete Cholesky conjugate gradient method. *Geophysical Journal International*,  
592 154(3), 947-956. <https://doi.org/10.1046/j.1365-246X.2003.02018.x>
- 593 Wu X., Xiao Y., Qi C. & Wang T., 2003. Computations of secondary potential for 3D DC  
594 resistivity modelling using an incomplete Choleski conjugate-gradient method.  
595 *Geophysical Prospecting*, 51(6), 567-577. [https://doi.org/10.1046/j.1365-](https://doi.org/10.1046/j.1365-2478.2003.00392.x)  
596 [2478.2003.00392.x](https://doi.org/10.1046/j.1365-2478.2003.00392.x)
- 597 Xu C., Dai M., You F., Shi X., Fu F., Liu R. & Dong X., 2011. An optimized strategy for real-  
598 time hemorrhage monitoring with electrical impedance tomography. *Physiological*  
599 *Measurement*, 32(5), 585-598.
- 600 Xu S.-z., Duan B.-c. & Zhang D.-h., 2000. Selection of the wavenumbers k using an optimization  
601 method for the inverse Fourier transform in 2.5D electrical modelling. *Geophysical*  
602 *Prospecting*, 48(5), 789-796. <https://doi.org/10.1046/j.1365-2478.2000.00210.x>
- 603 Xu S., Zhao S. & Ni Y., 1998. A boundary element method for 2-D dc resistivity modeling with a  
604 point current source. *Geophysics*, 63(2), 399-404. <https://doi.org/doi10.1190/1.1444339>
- 605 Yang J., Liu Y. & Wu X., 2017. 3-D DC resistivity modelling with arbitrary long electrode sources  
606 using finite element method on unstructured grids. *Geophysical Journal International*,  
607 211(2), 1162-1176. <https://doi.org/10.1093/gji/ggx356>
- 608 Zhang S., Xu G., Zhang X., Bo Z., Wang H., Xu Y., . . . Yan W., 2012. Computation of a 3-D  
609 Model for Lung Imaging With Electrical Impedance Tomography. *IEEE Transactions on*  
610 *Magnetics*, 48(2), 651-654. <https://doi.org/10.1109/TMAG.2011.2174779>
- 611